Chaos, Solitons and Fractals 182 (2024) 114851

Contents lists available at ScienceDirect

Chaos, Solitons and Fractals

journal homepage: www.elsevier.com/locate/chaos

Fingerprint pattern bi-turbulence in a driven dissipative optical system

P.J. Aguilera-Rojas [a], M.G. Clerc [a], S. Echeverría-Alar [a], Y. Soupart [b,*], M. Tlidi [b]

[a] Departamento de Física and Millenium Institute for Research in Optics, Facultad de Ciencias Físicas y Matemáticas, Universidad de Chile, Casilla 487-3, Santiago, Chile

[b] Département de Physique, Faculté des Sciences, Université libre de Bruxelles (U.L.B), C.P.231, Brussels, Belgium

ARTICLE INFO

Keywords:
Pattern dynamics
Chaos
Nonlinear optics
Liquid crystals light valve

ABSTRACT

Turbulence is a complex spatiotemporal behavior and a fundamental concept in fluid dynamics, which has been extended to other systems out of equilibrium, such as nonlinear optics, chemistry, active matter, and economics. Fingerprint patterns with sustained spatiotemporal dynamics in a liquid crystal light valve with an optical feedback experiment are studied. We show that the light intensity field presents a dynamical regime simultaneously exhibiting phase and amplitude turbulence. This bi-turbulent behavior of patterns is characterized by power-law spectra with exponents close to −2 and −3 spatially and −2 temporally, for the phase and amplitude respectively. The pattern orientation field also presents power-law spectra with exponents close to −2 and −3/4, spatially and temporally. We characterize the observed chaotic dynamics by estimating the largest Lyapunov exponent. We provide a theoretical model of pattern formation that explains the experimental observations with good qualitative agreement.

1. Introduction

Under the injection and dissipation of energy, macroscopic systems exhibit periodic spatial structures resulting from self-organization [1–3]. Often, these patterns emerge from a homogeneous steady state through spontaneous symmetry-breaking instabilities with an intrinsic wavelength. They have been observed in various fields of natural sciences, ranging from chemical, biological, and physical to optical systems (see recent overview [4]). As the bifurcation parameter increases, secondary instabilities give rise to more complicated but stationary patterns [2,3], such as quasi-crystals or disordered steady state patterns [3–7]. This issue has been extensively discussed and is now fairly well understood [1–4]. If the bifurcation parameter is further increased, patterns can exhibit complex spatiotemporal or turbulent type behaviors. Indeed, experiments supported by numerical simulations of various systems such as fluid convection [8], atmospheric, oceanic, and biological systems [9–13] show evidences of nonperiodic spatiotemporal dynamics. This feature was extended in other contexts, including fiber lasers [14–16], nonlinear optics [17], active matter [18,19], interfacial dynamics [20], chemical reactions [21], financial market features [22,23], and Bose–Einstein condensates [24]. In all these systems, the observed dynamics is of turbulent-like nature, that is, unpredictable, enhancing mixing properties, and involving a wide range of spatial wavelengths [9]. Classical turbulence exhibits power laws over several decades of wavenumber due to the different sizes of coherent structures, such as vortices. However, in other systems where turbulence-like behavior take place, a power law decay over one decade of wavenumber is typically observed in the power spectrum due to the absence of different coherent structures [14–23]. Theories such as weak turbulence, which accounts for the weak interaction of waves in various contexts, played a relevant role in the generalization of the notion of turbulence in "non-fluid" physical systems [25].

The statistical approach is the main technique used to characterize turbulence and turbulence-like behaviors, which yields relationships between coherent structures, defects, spatial modes, and waves present in the system. A prototype model for studying complexity is the two-dimensional complex Ginzburg–Landau equation, which accounts for oscillatory instabilities of homogeneous states [26]. This simple amplitude equation exhibits spatiotemporal behaviors such as phase and amplitude turbulence and spatiotemporal intermittency. Phase turbulence is characterized by power spectra with exponent −2 in the phase [27] and non-polynomial behavior in the amplitude. On the other hand, defect turbulence is characterized by power spectra of −5 in amplitude and −3 in phase [28]. A complementary approach to understand nonperiodic spatiotemporal chaotic evolution is to use dynamical systems tools such as Lyapunov exponents [29], which provides information about exponential sensitivity to initial conditions. Despite theoretical and experimental progress, combined statistical and dynamical studies of nonperiodic spatiotemporal patterns are scarce. For

* Corresponding author.
E-mail address: youri.soupart@ulb.be (Y. Soupart).

https://doi.org/10.1016/j.chaos.2024.114851
Received 6 March 2024; Accepted 6 April 2024

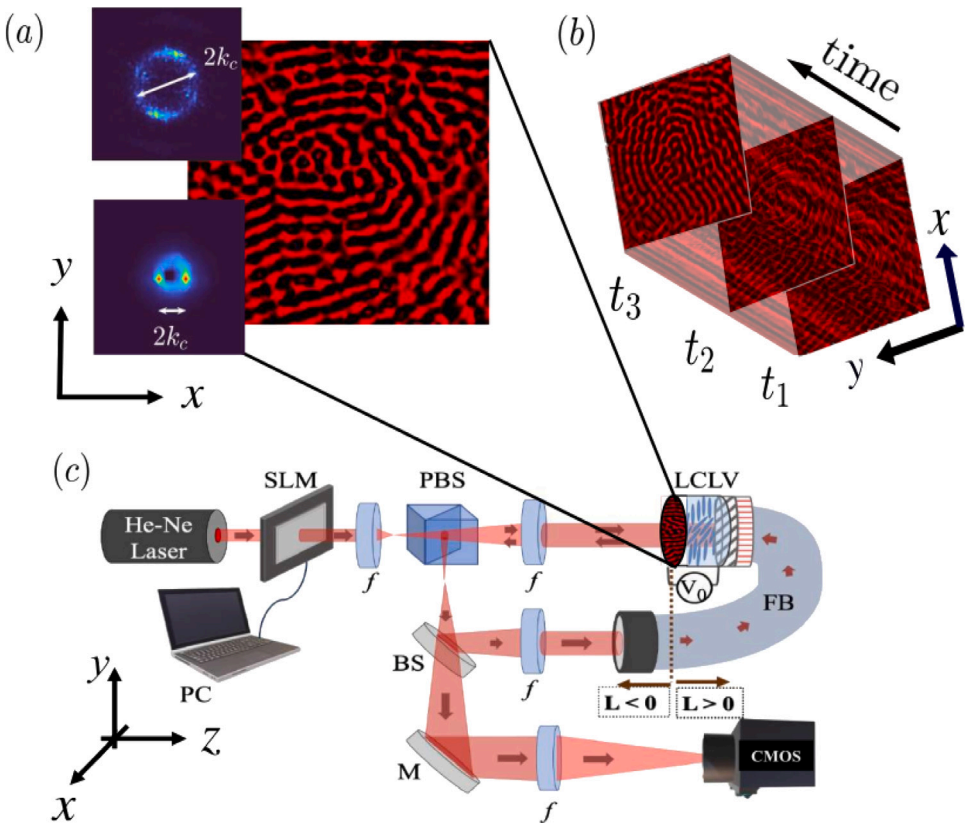

Fig. 1. Experimental observation of fingerprint pattern bi-turbulence. (a) Snapshot of bi-turbulent fingerprint pattern with the top inset accounting for the global Fourier transform averaged over time, showing a powder-like spectrum of typical wavenumber $k_0 \simeq 0.18\ \mu m^{-1}$. The bottom inset accounts for the spatiotemporal averaged windowed Fourier transform, highlighting the dominance of a single wavenumber k_c at short scales. We considered windows of size $2.2\ l_0$, where l_0 is the characteristic wavelength. (b) Spatiotemporal evolution of the disordered fingerprint patterns obtained for times $t_1 < t_2 < t_3$. Black color denotes zero intensity, and bright red denotes the highest intensity detected by the camera. (c) Schematic representation of a liquid crystal light valve (LCLV) with optical feedback, and its spatiotemporal evolution. The setup is composed of a coherent light source (He–Ne laser) sent through a spatial light modulator (SLM) and a polarizing beam splitter (PBS) before hitting the LCLV. After reflection, the light is brought to the fiber bundle (FB) with a beam splitter (BS) and to a complementary metal–oxide–semiconductor (CMOS) with a mirror (M). f represents achromatic lenses, and L is the free propagation length. The red arrows indicate the propagation of light.

example, experimental [8,13,14,16,21,24,30] or numerical [9,15] studies on nonperiodic patterns have been carried out in recent decades, but from a single perspective, statistical *or* dynamical.

Here, we evidence pattern bi-turbulence in a liquid crystal light valve (LCLV) with an optical feedback experiment (see Fig. 1). Pattern bi-turbulence is characterized by simultaneously presenting phase and amplitude turbulence. The light intensity field exhibits disordered fingerprint patterns with a sustained dynamics. Typical power-laws observed in the power spectra of the intensity field brought us to investigate the spatiotemporal evolution of the constitutive phase and amplitude fields. This led us to use statistical and dynamical tools to describe pattern bi-turbulence. *Statistically*, this dynamical behavior presents a spatial power spectrum law with a decay exponent close to -2 for the phase and -3 for the amplitude. Likewise, temporally, the phase and amplitude spectra present a power law close to -2. Note that the liquid crystal is a viscous and non-dispersive medium. The origin of phase turbulence is attributed to sharp jumps between spatial domains. Likewise, amplitude turbulence results from the constant nucleation and destruction of local defects and dynamics between them. Additionally, we compute the pattern orientation field, which accounts for the dynamics of the pattern wavevector, and show that its spatial and temporal power spectra are governed by power-laws with exponents close to -2 for the spatial spectrum and $-3/4$ for the temporal one. Statistical behaviors of light intensity fluctuations allow us to establish the intermittent nature of the dynamics, i.e., irregular alternations between different behaviors [9,10]. *Dynamically*, using the three-dimensional spatiotemporal evolution, we estimate the largest global and local Lyapunov exponents. These exponents suggest that the observed dynamics is chaotic. Finally, we discuss bi-turbulent patterns using a scalar model that describes the liquid crystal light valve with optical feedback close to the nascent of bistability and spatial instability. This scalar model exhibits qualitative agreement with the experimentally observed dynamics.

2. Pattern bi-turbulence: experimental observation

The liquid crystal light valve (LCLV) with optical feedback is a flexible experimental setup that exhibits a wide range of dynamical behaviors, such as multistability, front propagation, pattern formation, localized states, and nonperiodic spatiotemporal dynamics (see the review [31] and references therein).

2.1. Experimental setup

Fig. 1 shows a schematic representation of the LCLV with an optical feedback setup. The liquid crystal light valve consists of a nematic liquid crystal LC-654 (NIOPIK) with dielectric anisotropy constant $\epsilon_a = 10.7$ sandwiched between two glass layers separated by a distance $d = 15\ \mu m$. To apply an electrical voltage to the liquid crystals, transparent indium tin oxide (ITO) electrodes and a photoconductive layer are deposed on the glasses. A dielectric Bragg mirror with optimized reflectivity for 632.8 nm light is placed in the back layer of the liquid crystal cell. The molecules on the cell wall are attached parallel to it, corresponding to a planar anchoring in the diagonal direction of the cell. The LCLV can be electrically addressed by applying an oscillatory voltage V_0 rms and frequency $f_0 = 1.0\,kHz$ across the liquid crystal layer. The

optical valve is optically forced with a He–Ne laser, $\lambda = 632.8$ nm. The LCLV is placed in a $4f$ optical configuration ($f = 25$ cm), as indicated in Fig. 1. The optical feedback circuit is closed with an optical fiber bundle (FB) placed at a distance of $4f$ from the LCLV front face. The optical fiber bundle injects the light into the photoconductive layer, applying an additional local voltage to the liquid crystal material depending on the local light intensity. The optical feedback loop is designed so that light simultaneously presents diffraction propagation (characterized by the length L) and polarization interference induced by the polarizing beam splitter (PBS). A spatial light modulator (SLM) is considered to carry out two-dimensional or one-dimensional experiments with different geometries. The SLM prevents optical feedback in non-illuminated areas, generating an absorbing boundary condition. The experiment is monitored by a complementary metal–oxide–semiconductor (CMOS) camera.

2.2. Orientation field of the disordered pattern

The LCLV exhibits stationary hexagonal patterns when the valve is illuminated with a negative optical free propagation length L under a specific range of applied voltage V_0. The scenario shifts, leading to disordered spatiotemporal patterns when the voltage or free propagation length is increased. This behavior is illustrated in Fig. 1(a). The corresponding sustained spatiotemporal dynamics with defects is shown in Fig. 1(b); see video in the Supplementary Materials [32]. To characterize the observed pattern, we perform a Fourier analysis at each instant and average it over time to extract the spatial structure, evidencing a ring powder-like spectrum with a typical wavenumber $k_0 = 2\pi/l_0$ [see top inset in Fig. 1(a)]. This spectrum is a characteristic sign of disordered patterns, with a typical length but oriented in all directions [7]. Note that the aspect ratio is $\mathcal{L}/l_0 \simeq 17$, where $\mathcal{L}$ and l_0 are the system size and wavelength, respectively. To shed light on the local organization, we compute the averaged windowed Fourier transform [see bottom inset in Fig. 1(a)] [5,32]. The spatial averaged windowed Fourier transform technique is described in Appendix A. From this analysis, one concludes that the pattern is of the labyrinthine or fingerprint type; that is, a single spatial mode with a wavenumber around k_0 dominates the local dynamics of the patterns. Hence, we can define a local wave vector $\vec{k}(x, y, t)$ and its corresponding pattern orientation phase $\varphi(x, y, t)$ with respect to the horizontal direction [33]. We use a local approximation of the intensity field of the form $I(\vec{r} = \{x, y\}, t) \approx A\cos[\varphi(\vec{r}, t)]$ where A and φ are the amplitude and phase. The associated local wave vector is $\vec{k}(\vec{r}) \equiv \vec{\nabla}\varphi(\vec{r})$. It is then possible to build the pattern orientational field $\varphi(\vec{r}) = \arctan[k_y(\vec{r})/k_x(\vec{r})]$ being the angle of the wave vector with respect to a given direction (here, the horizontal one). To soften the orientational field, a Gaussian filter of parameter $l_0 = 2\pi/k_0$ is applied where k_0 is the critical wavenumber of the pattern. Fig. 2(b) shows the orientational field φ associated with the respective disordered patterns. The spatial power spectrum is taken as the squared Fourier transform of the time-averaged of the orientation field while temporal power spectra have been averaged over 10,000 points. Figs. 2(c) and 2(d) show these power spectra as a function of the wavenumber k and frequency ω, where k is the radial wavenumber of the field averaged azimuthally. These charts provide evidence of power-law tails close to k^{-2} and $\omega^{-3/4}$, respectively. This experimental result indicates the turbulent-like nature of the observed disordered pattern. The exponent -2 suggests a phase turbulence in the orientation field. Phase turbulence is a dynamical behavior first discovered numerically for coupled oscillators by Kuramoto [27,34], and later Manneville for an equivalent phase model numerically establishes a power law for the power spectrum [35]. Analytical explanations for this behavior were proposed in Refs. [36,37]. The origin of the exponent corresponds to non-correlated abrupt transitions between two typical values of the phase; see inset of Fig. 2(c) [38,39]. Then, the tail of the power spectrum is dominated by sharp jumps of the phase. Those can be approximated by a translated Heaviside function, $H(x - x_0)$, such that

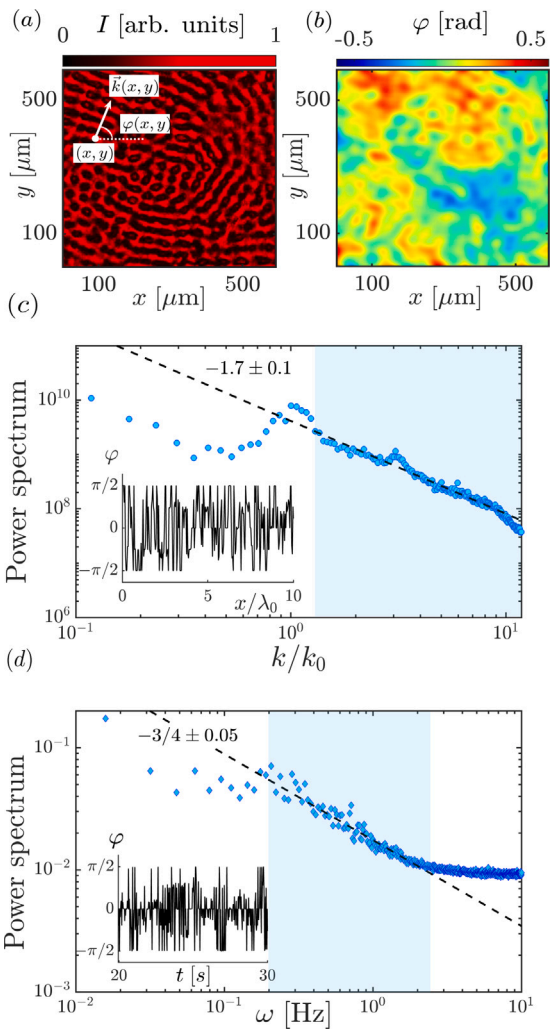

Fig. 2. Orientation domains of the disordered patterns: characterization and dynamics. (a) Snapshots of the light intensity $I(x, y, t)$ and (b) the respective orientation field $\varphi(x, y)$. The white arrow shows the local wavevector $\vec{k}(x, y, t)$ orthogonal to the local stripe pattern and forming an angle $\varphi(x, y, t)$ with respect to the horizontal direction. (c) Spatial power spectrum of the orientation field φ. k_0 is the intrinsic wavenumber of the pattern. The full line $k^{-2.0\pm0.1}$ accounts for the power-law behavior of the tail, while the dashed line $k^{-1.7\pm0.1}$ is a fit considering more data points from the power spectrum. The inset shows a one-dimensional spatial cut. (d) Temporal power spectrum. The dashed line $\omega^{-3/4\pm0.05}$ describes the power-law regime before the noise-induced flattening of the curve. The inset shows the temporal evolution measured at a single point.

$\varphi_{jump}(x, t) = \varphi_0 + \Delta\varphi H(x - x_0)$, where φ_0 and $\Delta\varphi$ are constants. The power spectrum of these function decays as k^{-2}. In fluids, the power spectra exhibit several decades of wavenumber as a result of the interaction of coherent structures (eddies) of different scales [10]. In the case of disordered patterns, the coherent structures driving the turbulence are local defects, which have a size of the order of l. Therefore, the turbulent window of the spectrum cannot cover a wide range of wavenumbers.

Because the system lacks a dispersion relationship, spatial and temporal spectra are not directly related (cf. Fig. 2). The exponent close to -0.75 is due to the different states that the orientational field explores. Note that the temporal power spectrum for large frequencies deviates from the power law and tends to flatten out. This phenomenon is due to the effect of noise inherent in the experimental system, such as thermal and electronic fluctuations in the control elements [40].

In brief, we observed nonperiodic spatiotemporal dynamics for the orientational field characterized by a phase turbulence type of behavior. As for the orientation field, the observation of a power-law

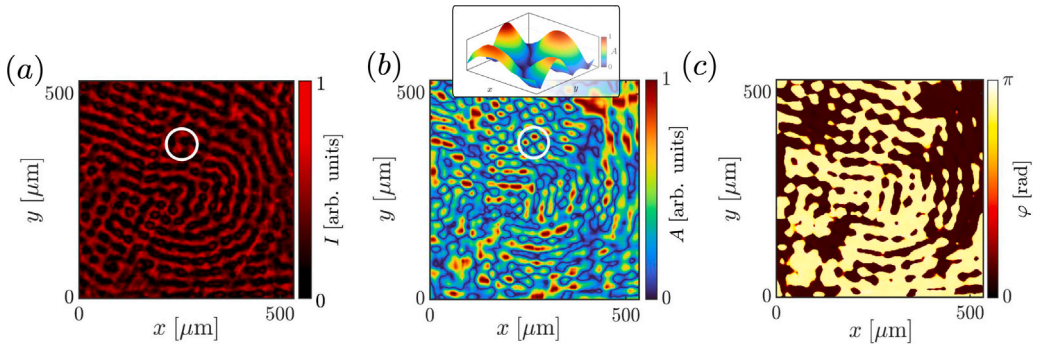

Fig. 3. Amplitude and phase of the fingerprint pattern. (a) Instantaneous intensity field and corresponding amplitude (b) and phase (c) computed using the generalized Hilbert transform. The white rings illustrate the position of a defect. The inset in (b) accounts for the surface plot of an amplitude defect. The color bar shows the respective values of fields. (For interpretation of the references to color in this figure legend, the reader is referred to the web version of this article.)

spectrum for the measured intensity field motivated us to analyze in more details the experimental result by studying separately the phase and amplitude fields of the pattern.

2.3. Analysis of amplitude and phase of the disordered pattern

One can obtain the instantaneous amplitude $A(\vec{r},t)$ and phase $\phi(\vec{r},t)$ of the disordered pattern through the generalized Hilbert transform [41]. This method is described in Appendix B. This transformation allows us to separate the pattern dynamics into two scalar fields that provide information about the envelope of the pattern and its respective phase, which is a useful technique for the analysis of signal and telecommunications. Fig. 3 depicts a typical snapshot of the disordered pattern and the corresponding amplitude and phase fields, respectively. We perform spatial and temporal statistical analysis from these fields. Fig. 4 shows the respective spatial power spectra. The phase ϕ presents similar dynamical behavior to that obtained for the pattern orientation φ, namely the k^{-2} decay characteristic of phase turbulence. Unexpectedly, for the pattern amplitude A, we find that the critical behavior of the power spectrum tail is close to k^{-3}. It is well-known that local singularities or defects arising from nonlinear evolution produce power-law tails in the short-wavelength turbulence spectrum [38,39]. Notice the amplitude presents local defects responsible for having the exponent −3. This is because the amplitude vanishes linearly at the core of the defect and decays exponentially away from it. A local defect and its amplitude profile is highlighted with a white ring in Fig. 3. Hence, the system exhibits patterns with phase and defect turbulence simultaneously, *pattern bi-turbulence*. Prototype complexity models, such as the complex Ginzburg–Landau equation, show these behaviors in a disjoint way [26]. Experimentally, we show that the amplitude and the intensity field are characterized by similar power-laws (see Fig. 4).

In this subsection, the analysis provides information on the spatial behavior of the dynamical patterns. Because the liquid crystal is an overdamped system, it does not present a wave dispersion relation. Namely, dynamics are not driven by waves. Thus, temporal analysis can also provide information on the coupling between modes and defects. We consider a spatial point in the system, calculate its temporal Fourier transform, and then spatially average over all information points. Fig. 5 gathers the power spectra found for intensity, amplitude, and phase in the frequency domain. In all these spectra, we find exponents for the tails close to −2. Hence, temporal dynamics are characterized by exhibiting abrupt changes that are not correlated with each other (cf. insets in Fig. 5). As in Fig. 2 we observe that the power spectra deviate from the power laws for large frequencies.

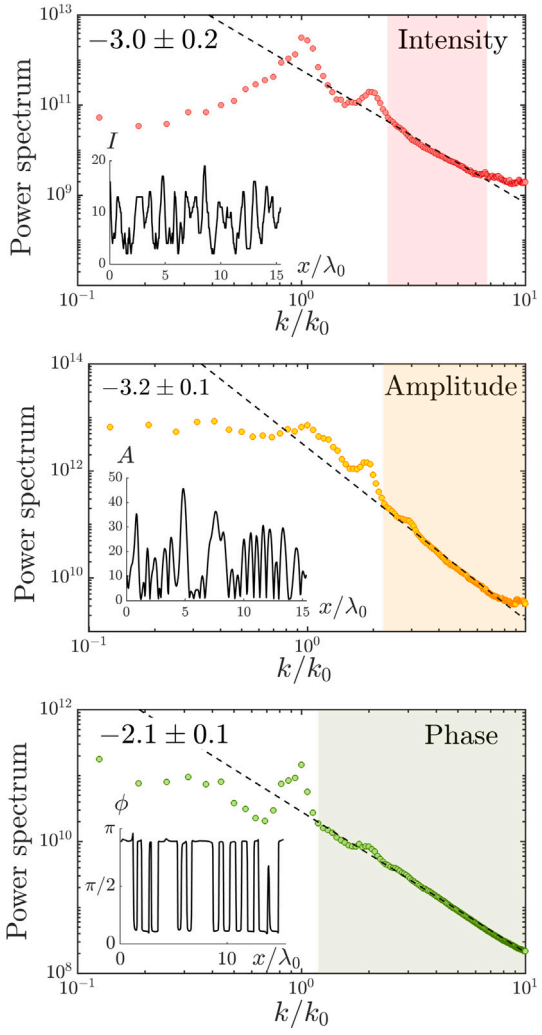

Fig. 4. Spatial power spectra of intensity (○), amplitude (○), and phase (○). Dashed lines account for the power-law tendencies of the tails. The critical exponents are determined by fitting the tails of the spectra, and minimum squares determine the error. Insets: one-dimensional spatial cuts in the respective fields. (For interpretation of the references to color in this figure legend, the reader is referred to the web version of this article.)

2.4. Characterization of the spatial and temporal fluctuations

Due to their deterministic character, turbulent fields present fluctuations near equilibrium that have non-Gaussian behavior [10], as shown in Fig. 6. We observe that the fluctuations do not follow a Gaussian law characteristic of additive white noise processes, in accordance with the deterministic character of the observed dynamics. To better understand

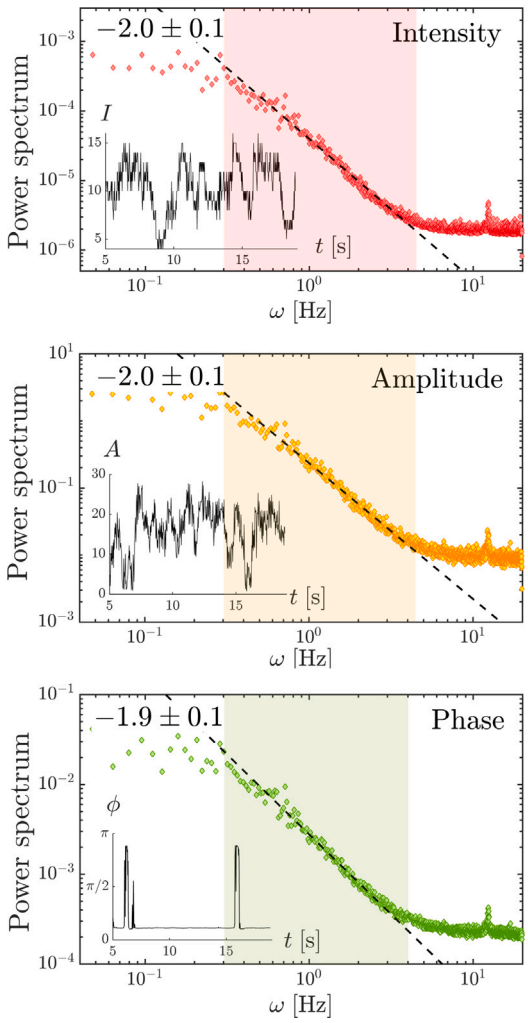

Fig. 5. Temporal power spectra of intensity (◇), amplitude (◇), and phase (◇). Dashed lines account for the power-law tendencies of the tails. The critical exponents are determined by fitting the tails of the spectra, and minimum squares determine the error. Insets: one-dimensional temporal cuts in the respective fields. (For interpretation of the references to color in this figure legend, the reader is referred to the web version of this article.)

the fluctuations and if they have characteristic scales, one can study the higher-order correlations, also called *structure functions* [10], defined at order p as $S_p(\tau) \equiv \langle \|I(t_0) - I(t_0+\tau)\|^p \rangle$, where the symbol $\langle\rangle$ accounts for the temporal average. For self-similar turbulent fluid dynamics, Kolmogorov theory predicts a scaling law of type $S_p(\tau) \propto \tau^{\zeta_p^\tau}$, with $\zeta_p^\tau = p/3$ [10]. This means the system does not have characteristic scales in the turbulent window. Discrepancies from this law account for intermittent behavior and the breaking of self-similarity. Using the structure functions, we have determined the evolution of the scaling exponents with the order p. Fig. 7 summarizes the observed results. The temporal exponent has been computed from a linear fit in the turbulent window of the structure functions. We observe that a close to $p/6$ law is well followed until order 4, from which the curve bends away. Therefore, the light intensity exhibits intermittent behavior (see Fig. 7a). To illustrate this dynamical behavior, we show profiles of the moments m_p for different exponents p in the insets of Fig. 7a, where $m_p \equiv \langle (I(t) - \langle I \rangle)^p \rangle / \sigma^p$, $I(t)$ and $\langle I \rangle$ are the total intensity at time t and average intensity, and σ is the standard deviation. From these charts, we can clearly observe the loss of self-similarity at large p and the intermittent behavior (see also inset of the top panel of Fig. 5). A similar analysis can be performed for spatial fluctuations.

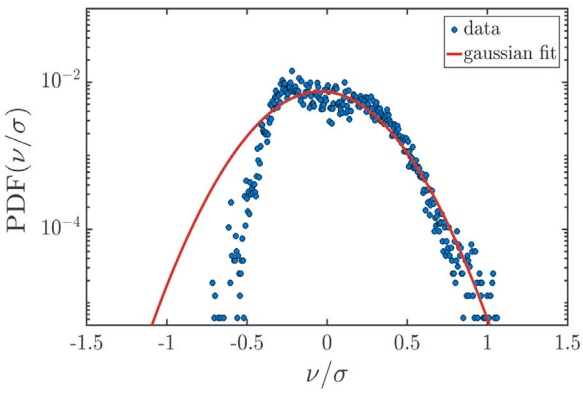

Fig. 6. The probability density function of the normalized experimental intensity fluctuations ν (circles) is compared with a Gaussian fit (full line), where σ is the standard deviation.

Fig. 7b shows the behavior of ζ_p^r exponent as a function of p, where spatial structure function satisfies $S_p(r) \equiv \langle \|I(r_0) - I(r_0+r)\|^p \rangle \propto r^{\zeta_p^r}$, with r the radial coordinate. We observe a precise self-similarity along the computed linear curve, as indicated by the profiles of the spatial moments for different values of p (see insets). Those are defined by $m'_p = \langle (I(r) - \langle I \rangle)^p \rangle / \sigma^p$, where $I(r)$ is the total intensity at position r. We infer that the spatial turbulent behavior is not intermittent, as first suggested by the inset of the top panel of Fig. 4. Hence, the turbulent patterns are self-similar in space but not in time. Notably, the nonperiodic spatiotemporal behavior differs from traditional fluid and weak turbulence.

2.5. Chaotic dynamics: experimental characterization

From the theory of dynamical systems, one of the main turbulence features is its exponential unpredictability [9], i.e., its sensitivity to initial conditions characterized by the Lyapunov exponents [29]. Spatial and temporal power spectra are indicators of complex spatiotemporal dynamics (strange attractors); however, complex behaviors such as quasi-periodicity and behaviors with polynomial sensitivity are not chaotic [42]. Due to the experimental difficulties inherent in establishing the Lyapunov spectrum [43], we can only measure the largest global and local Lyapunov exponents. By considering different slices in the spatiotemporal diagram, one can determine the largest Lyapunov exponents [43].

Fig. 8a shows a two-dimensional section of the spatiotemporal dynamics (spatiotemporal slice) of disordered patterns, from which two excerpts with similar initial conditions are extracted (see Fig. 8b). The local largest Lyapunov exponents $\{\lambda_{max}(x), \lambda_{max}(y)\}$ are determined using the expressions

$$\lambda_{max}(x) = \frac{1}{T} \frac{\|I(x,y,T) - I'(x,y,T)\|_x}{\|I(x,y,t_0) - I'(x,y,t_0)\|_x},$$
$$\lambda_{max}(y) = \frac{1}{T} \frac{\|I(x,y,T) - I'(x,y,T)\|_y}{\|I(x,y,t_0) - I'(x,y,t_0)\|_y}, \quad (1)$$

where $I(x,y,t)$ and $I'(x,y,t)$ account for the intensity of light in the different excerpts. T is the elapsed time in the temporal window long enough to characterize the spatiotemporal dynamics. The symbols $\|\cdot\|_x$ and $\|\cdot\|_y$ account for the integration along the y- and x-direction, respectively. We integrate the spatiotemporal evolution over the different slices to understand the spatial sensitivity to initial conditions, obtaining the local largest Lyapunov exponents depending on the slice position (see Fig. 8c). From these local largest Lyapunov exponents, we extract the global largest Lyapunov exponent λ_0 as the mean value of the local ones. We get $\lambda_0 = 0.009 \pm 0.006\ s^{-1}$. Note that the global largest

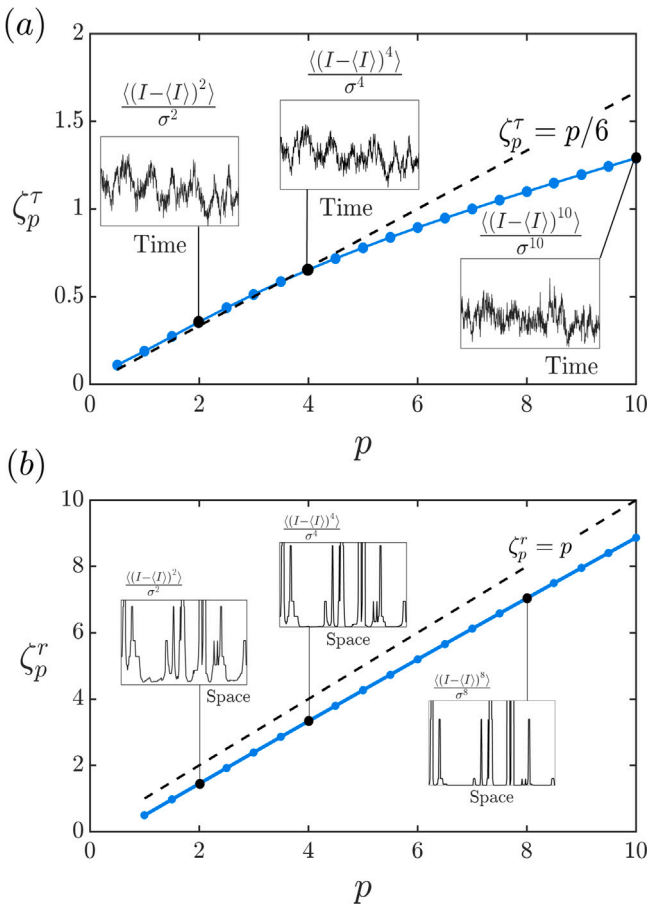

Fig. 7. Temporal intermittency and spatial self-similarity. (a) Scaling exponents ζ_p^τ of the temporal structure functions $S_p(\tau) \equiv \langle \|I(t_0) - I(t_0+\tau)\|^p \rangle \propto \tau^{\zeta_p}$ as a function of p. The blue points are obtained from the experimental data, and the blue curve allows us to visualize their trend. The dashed line shows a scaling of $p/6$ and emphasizes the deviation from it. Insets accounts for the temporal evolution of the moments $m_p = \langle (I(t) - \langle I\rangle)^p \rangle / \sigma$ where $I(t)$ and $\langle I$ are, respectively, the total intensity at time t and the average intensity, and σ is the standard deviation. (b) Spatial scaling exponents ζ_p^r of the spatial structure functions $S_p(r) \equiv \langle \|I(r_0) - I(r_0+r)\|^p \rangle \propto r^{\zeta_p^r}$ as a function of p. The blue points are obtained from the experimental data, and the blue curve allows us to visualize their trend. The dashed line shows a scaling of $\zeta_p^r = p$. Insets accounts for the spatial variation of the moments $m_p = \langle (I(r) - \langle I\rangle)^p \rangle / \sigma$ where $I(r)$ and $\langle I\rangle$ are the total intensity at position r and the average intensity and σ is the standard deviation. (For interpretation of the references to color in this figure legend, the reader is referred to the web version of this article.)

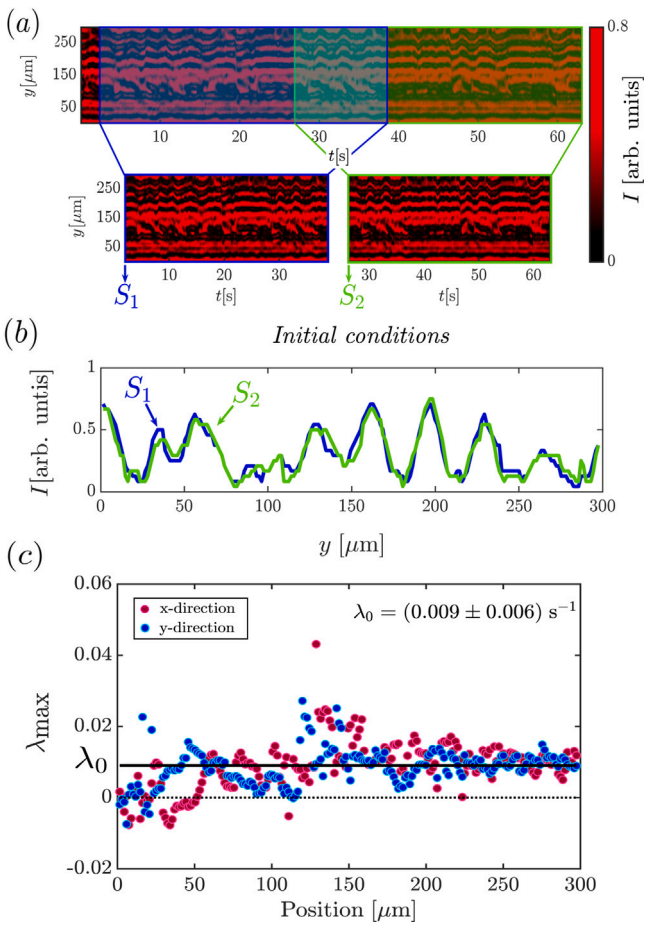

Fig. 8. Experimental largest Lyapunov exponents. (a) Two-dimensional section of spatiotemporal dynamics of the disordered fingerprint patterns. The bottom panels are two excerpts with similar initial conditions. (b) Profile of the initial conditions for the different excerpts. (c) The local largest Lyapunov exponents λ_{max} are measured for the respective local spatiotemporal slide extending in the respective direction. The black line accounts for the global largest Lyapunov exponent $\lambda_0 = 0.009 \pm 0.006$ s^{-1}. (For interpretation of the references to color in this figure legend, the reader is referred to the web version of this article.)

Lyapunov exponent value is the same in each direction. As a result, the disordered patterns under investigation are chaotic, i.e., exponentially sensitive to initial conditions.

The characteristic predictability time of the system is of the order of one minute ($1/\lambda_0$). Therefore, the dynamics of the pattern are slow compared to the typical temporal dynamics of the LCLV, which is of the order of milliseconds. Hence, from Fig. 8c, the observed dynamical behavior is of a chaotic nature. Because of the inherent heterogeneities in the experiment, it can also be deduced from this chart that the sensitivity to the initial conditions depends on the perturbed region. Imperfections are responsible for nucleation or trapping pattern defects. We have considered different spatial regions of the LCLV and observed a similar bi-turbulent behavior.

3. Theoretical description of disordered fingerprint patterns

Due to optical feedback, the dynamics of the liquid crystal molecular average orientation field is nonlocal in space and local in time. Then, its dynamic behavior is difficult to understand. To shed light on the pattern dynamics from a theoretical point of view, we study the LCLV simultaneously close to nascent bistability *and* spatial instability. In the neighborhood of this so-called *Lifshitz critical point* [44–46], the system can be described by the non-variational Swift–Hohenberg equation

$$\partial_t u = \eta - \beta u^3 - \nu \nabla^2 u - \nabla^4 u + \kappa (\nabla u)^2 \nabla^2 u, \tag{2}$$

where the scalar field $u = u(\vec{r}_\perp, t)$ accounts for the angular deviation from the critical average orientation angle θ_c at the Lifshitz critical point and $\vec{r}_\perp = (x, y)$ stands for transversal coordinates [46]. η is the control parameter and accounts for the asymmetry between the bistable states. The cubic term accounts for the nonlinear saturation of the system ($\beta > 0$). ν characterizes resultant (anti) diffusion effect when it is (positive) negative. This term accounts for the balance between the liquid crystal diffusion and the feedback light diffraction effect. Note that ν is negative when diffusion is dominant. The $\nabla^2 = \partial_{xx} + \partial_{yy}$ is the Laplace operator acting on the transverse plane (x, y). The fourth term, $\nabla^4 u$, stands for the hyperdiffusion; which is a term that describes the stabilization of large spatial gradients and tends to homogenize the system. When the system exhibits anti-diffusion, the characteristic length of the pattern $k_0 = \sqrt{\nu}$ is determined by the balance between anti-diffusion and hyper-diffusion. The last term is non-variational and accounts for nonlinear diffusion. The complete and extensive expressions of the coefficients, based on the LCLV parameters, and their derivation in a more general form can be found in Ref. [47].

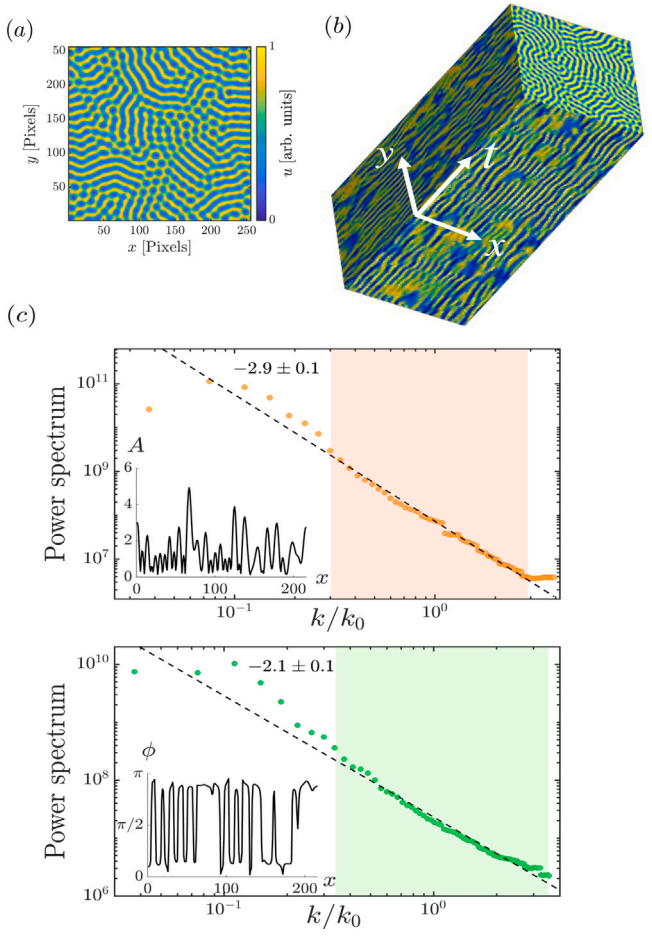

Fig. 9. Numerical bi-turbulent pattern obtained from non-variational Swift-Hohenberg Eq. (2) with $\eta = 0.03$, $\beta = 0.01$, $\nu = 0.5$, and $\kappa = -0.1$. (a) Colormap of the scalar field $u(x, y, t)$ at given time. (b) Spatiotemporal diagram of the disordered pattern. (c) Power spectra of the amplitude (○) and phase (○) of the bi-turbulent patterns. Straight lines account for the power-law tendency of the tails in the power spectra. Insets: one-dimensional spatial cuts in the respective scalar fields. (For interpretation of the references to color in this figure legend, the reader is referred to the web version of this article.)

Similar scalar models as Eq. (2) have been derived in many contexts of nonlinear science, including optics, chemistry, and biology, and are frequently referred to as nonvariational Swift-Hohenberg equations [44–46,48]. Besides, these types of non-variational equations have been proposed to explore stripe patterns far from equilibrium [49,50]. The model (2) accounts for bistability between homogeneous states, periodic solutions, fronts between these states, localized structures, and spatiotemporal chaos, among other dynamical behaviors. In a particular region of parameters, the model Eq. (2) presents disordered fingerprint patterns with sustained dynamics (cf. Fig. 9). Notice that the dynamics of the disordered fingerprint patterns are qualitatively similar to that observed experimentally, that is, a sustained dynamics of the defects is observed on the disorder patterns. Based on the generalized Hilbert transform [41], we can characterize the pattern phase and amplitude dynamics. Fig. 9 summarizes the numerical findings obtained. From this chart, we can infer that the model Eq. (2) exhibits patterns bi-turbulence. Hence, the obtained dynamics behaviors agree with the experimental observations. All numerical simulations are performed without taking into account material imperfections. In spite of this approximation, the system exhibits pattern bi-turbulence (see Fig. 9).

Numerical integrations of the model Eq. (2) are implemented by using a pseudospectral code in a 256 × 256 square simulation box with periodic boundary conditions and a spatial discretization $dx = dy = 0.8$. The temporal integration is performed with the Runge–Kutta order-4 algorithm with a time-step $\Delta t = 0.1$. The initial conditions are numerically prepared static disordered patterns.

To characterize the nature of the observed dynamics, we have considered a smaller integration domain (128 × 128). The Lyapunov spectrum can be determined numerically. In Appendix C, the numerical method to calculate the Lyapunov spectrum is detailed. Fig. 10 shows the Lyapunov spectrum associated with pattern bi-turbulence along with the four most unstable eigenvectors. The most unstable modes are dominated by defects as shown in Fig. 10 where two domain walls drive the nonperiodic dynamics. To illustrate the role of defects near the region of spatiotemporal chaos emergence, we observe that the dynamics is driven by a small number of dislocations. Fig. 11 shows the Lyapunov spectrum with only two unstable modes and the corresponding eigenvectors. We can see the influence of defects in the most unstable eigenvector modes. In brief, the numerically computed dynamics is spatiotemporal chaotic in nature.

4. Conclusions

We have considered an experimental set-up based on the liquid crystal light valve with optical feedback in two-dimensional settings. We investigated the formation of spatiotemporal waveless fingerprint patterns far from the onset of primary symmetry-breaking instabilities, experimentally and theoretically. We performed a complete characterization combining statistical and dynamical approaches.

Using statistical tools, such as averaged global and local windowed Fourier transforms, power spectral densities, fluctuations distributions and higher order cumulants (structure functions), we characterized the spatial and temporal behaviors of the system. From the local wave vector of the pattern, we constructed the orientation field and showed evidence of a power-law decay in the associated temporal and spatial power spectra. From the spatial exponent close to −2, we infer that this orientation field's dynamics undergoes a phase turbulence. We also observed a power-law decay in the recorded intensity field with exponents close to −3 in space and −2 in time. Further, we have addressed the question whether this observed behavior is due to the well-known phase or amplitude turbulence regime. For this purpose, we separated the intensity field into constitutive amplitude and phase fields by using a generalized Hilbert transform in two dimensions. Performing a similar analysis, we have shown that the spatial power spectra possess power-laws with exponents close to −2 for the phase and −3 for the amplitude. For the temporal spectra, these exponents are −2 for both the phase and the amplitude. These results suggested that the experimentally recorded signal support simultaneously both phase and amplitude turbulence. We coined this behavior pattern bi-turbulence. In addition, we have shown that the fluctuations followed non-Gaussian statistics and, by means of temporal and spatial structure functions, we evidenced the intermittent nature of the temporal dynamics.

Using dynamical tools such as Lyapunov largest local and global exponents, we established the exponential sensitivity to initial conditions which is typical for a chaotic nature of the observed dynamical pattern. We found that the dynamics is characterized by a Lyapunov exponent $\lambda_0 = 0.009\ \mathrm{s}^{-1}$. Due to spatial inhomogeneities that are inherent to the liquid crystal material, we have considered different spatial regions of the liquid crystal and observed similar bi-turbulent behavior.

By using combined statistical and dynamical approaches, we were able to conduct a thorough analysis of the observed dynamical patterns and to highlight many of its features such as the simultaneous phase and amplitude turbulence, i.e., pattern bi-turbulence, and its intermittent and chaotic nature. To support these experimental findings, we investigated through theoretical description of the liquid crystal light valve with optical feedback, the formation of two-dimensional patterns far from the symmetry-breaking instability. The theoretical predictions were in good qualitative agreements with the experimental observations.

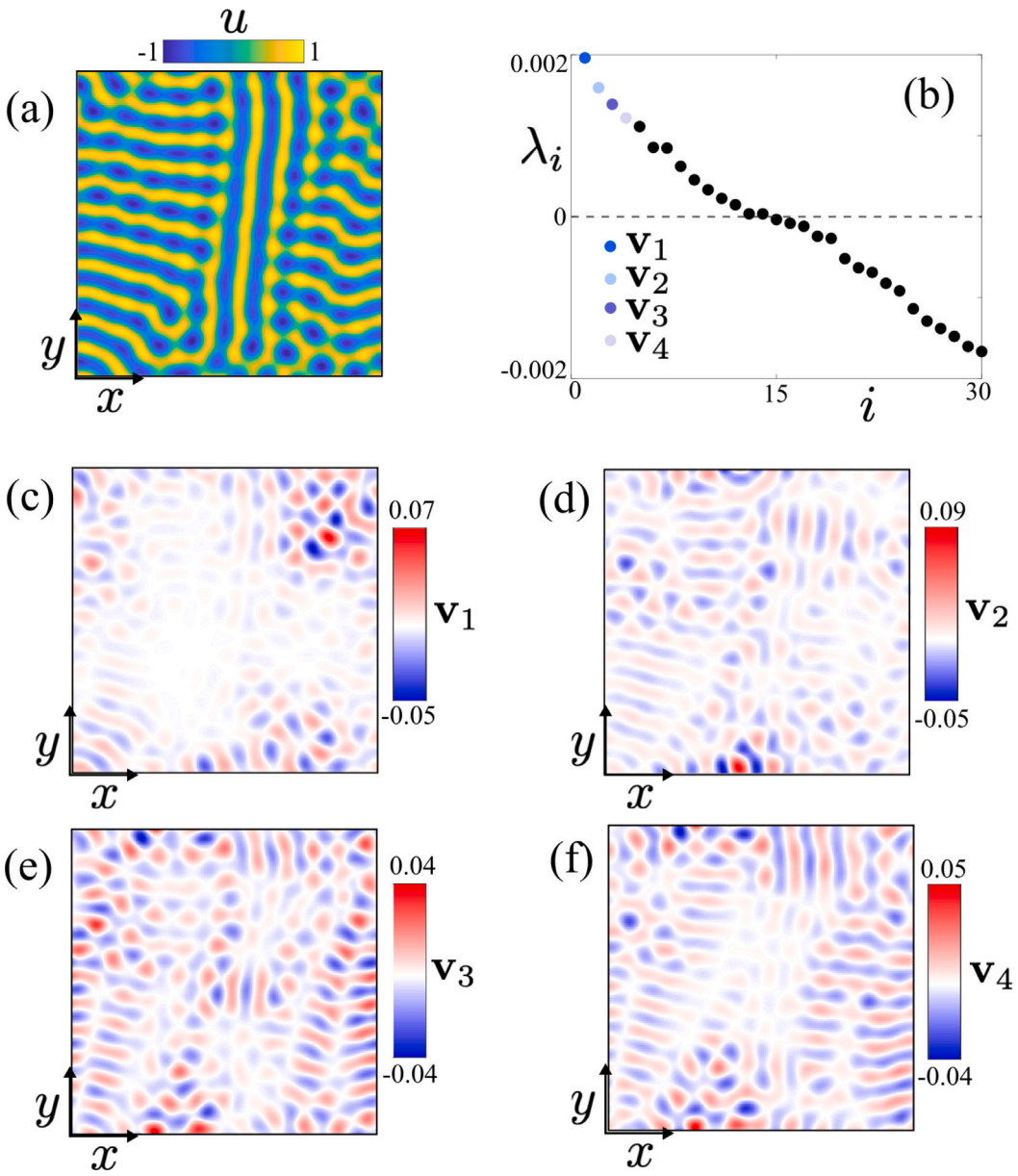

Fig. 10. Chaotic dynamics of a bi-turbulent pattern obtained from model Eq. 9 with $\eta = 0.03$, $\nu = -0.5$, $\beta = 0.01$, and $\kappa = -0.1$. (a) Snapshot of a typical numerical disordered pattern, (b) Lyapunov spectrum (the first 30 exponents of the associated Lyapunov spectrum), and (c)–(f) largest eigenvectors Lyapunov modes, where the lowest index is associated with the most unstable mode, respectively.

Complex spatiotemporal dynamics are common in driven dissipative out-of-equilibrium systems such as in biology, chemistry, nonlinear optics, active matter, financial markets, and Bose–Einstein condensates. The strategy of considering auxiliary fields such as phase, amplitude, and orientation field, rather than the directly measured physical variable, provides a systematic framework for identifying and classifying nonperiodic spatiotemporal phenomena from disordered patterns observed in various nonequilibrium systems.

CRediT authorship contribution statement

P.J. Aguilera-Rojas: Data curation, Writing – review & editing. **M.G. Clerc:** Conceptualization, Funding acquisition, Investigation, Supervision, Writing – original draft, Writing – review & editing. **S. Echeverría-Alar:** Investigation, Software, Writing – review & editing. **Y. Soupart:** Investigation, Software, Writing – review & editing. **M. Tlidi:** Writing – review & editing.

Declaration of competing interest

The authors declare the following financial interests/personal relationships which may be considered as potential competing interests: Youri Soupart reports financial support was provided by Millenium Institute for Research in Optics (MIRO). If there are other authors, they declare that they have no known competing financial interests or personal relationships that could have appeared to influence the work reported in this paper.

Data availability

Data will be made available on request.

Acknowledgments

The authors are thankful for fruitful discussions with C. Falcón. P.J. A-R, M.G.C. S.E.-A, and Y.S. are thankful for the financial support of

ANID-Millenium Science Initiative Program-ICN17_012, Chile (MIRO) and FONDECYT, Chile Project No. 1210353. S.E.-A. acknowledges the financial support from ANID by Beca Doctorado Nacional, Chile 2020-21201376. M. Tlidi acknowledges financial support from the Fonds National de la Recherche Scientifique (Belgium) under Grant CDR No. 35333527 "Semiconductor optical comb generator".

Appendix A. Spatial averaged windowed Fourier transform

The spatial averaged windowed Fourier transform characterizes the short-range order of the pattern [5]. This is achieved by partitioning the original image under study into small boxes on scales larger than the length of the pattern and smaller than the scale at which the disordered pattern is observed. Then, the scale of small boxes must be such that their Fourier transform must be qualitatively different from the global Fourier transform. We consider a large number of boxes of the same length l, calculate the Fourier transform, rotate the wave-vector space so that a peak of the transformation is always horizontal and average over these windowed transforms. Note that the boxes can be taken in a random or ordered manner. In this study, we focus only on regular partitions. Differentiating between different globally disordered patterns is made possible by the spatial averaged windowed Fourier transform.

Appendix B. Generalized Hilbert transform

We used a generalized Hilbert transform method to extract the amplitude $A(x, y)$ and phase $\phi(x, y)$ fields from the 2D patterns observed in the experiment and the numerical simulations [41]. This formalism allows filtering the characteristic wavelength λ of the 2D patterns in a rotational invariant manner. The procedure supposes that the 2D spatial signal (pattern) $u(x, y)$ behaves locally as a curved stripe pattern with amplitude A, direction θ, curvature κ, and phase ϕ. The whole pattern is embedded into a 3D conformal space to perform the generalized Hilbert transform. For numerical simplicity, this space is chosen as a sphere [41]. Then, the algorithm is a 2D convolution on a sphere. The convolution *filter* size is 2λ. This choice is related to the size of defects, which on average is between λ and 2λ in the experiment and the numerical simulations. Finally, the local features of the patterns (A and ϕ in our case) are extracted by angular change of variables on the sphere. In the numerical simulation, after the Hilbert transform, the amplitude and the phase fields are filtered with a Gaussian width function $\lambda/2$ to eliminate higher harmonic effects.

Appendix C. Lyapunov spectrum from the numerical model

The spatiotemporal dynamics exhibited by the bi-turbulent patterns (solution $\bar{u}$ of Eq. (2)) can be characterized with a by number (n) of Lyapunov exponents λ_i ($i = 1, \dots, n$), where $\lambda_i > 0$ is a feature of chaos.

Part of the Lyapunov spectra was obtained by following the numerical procedure detailed in [51]. Several perturbations (n) around $\bar{u}$ are performed and then monitored on time. Each perturbation is governed by the linearized equation $\partial_t \delta\mathbf{u} = \mathbf{J}(\bar{u})\delta\mathbf{u}$, where $\delta\mathbf{u}$ is a perturbation around the solution $\bar{u}$ and $\mathbf{J}(\bar{u})$ is the respective discretized Jacobian. Considering n orthonormal vectors $\mathbf{v}_i$ (perturbations) with d elements, where d is the dimension of the dynamical system, one can introduce the matrix $\mathbf{L}(t_o) = [\mathbf{v}_1 \dots \mathbf{v}_n]$. The temporal evolution of $\mathbf{L}$ after a time increment dt is $L(t_o + dt) = e^{dt\mathbf{J}}\mathbf{L}(t_o)$. In each time step, the modified Gram–Schmidt **QR** decomposition is performed on $L(t_o + dt)$, and the diagonal elements of $\mathbf{R}$ are recorded. After repeating

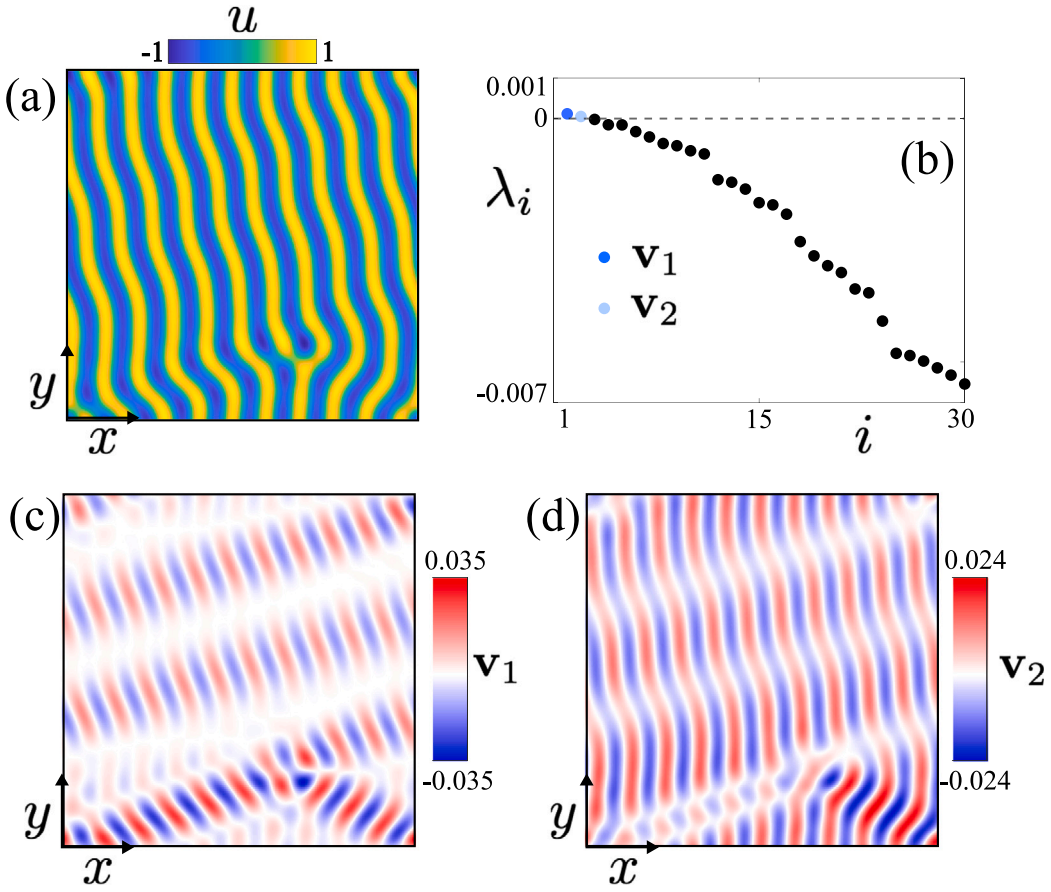

Fig. 11. Chaotic dynamics of model Eq. 9 close to emergence of spatiotemporal chaos. (a) Snapshot of a dislocations dynamics, (b) Lyapunov spectrum (the first 30 exponents of the associated Lyapunov spectrum), and (c) largest eigenvectors Lyapunov modes, where the lowest index is associated with the most unstable mode, respectively.

the previous algorithm for N iterations, the Lyapunov exponents can be approximated by

$$\lambda_i = \frac{1}{N dt} \sum_{k=1}^{N} \ln[\mathbf{R}_{ii}(t_o + kdt)], \tag{C.1}$$

when N is sufficiently large.

References

[1] Nicolis G, Prigogine I. Self-organization in non equilibrium systems. New York: Wiley; 1977.
[2] Pismen LM. Patterns and interfaces in dissipative dynamics. Berlin: Springer; 2006.
[3] Cross M, Greenside H. Pattern formation and dynamics in nonequilibrium systems. New York: Cambridge University Press; 2009.
[4] Tlidi M, Clerc M, Panajotov K. Dissipative structures in matter out of equilibrium: from chemistry, photonics and biology (part 1). Philos Trans R Soc A 2018;376:20180114.
[5] Echeverría-Alar S, Clerc MG. Labyrinthine patterns transitions. Phys Rev Res 2020;2. 042036(R).
[6] Newell AC, Pomeau Y. Turbulent crystals in macroscopic systems. J Phys A 1993;26:L429.
[7] Le Berre M, Ressayre E, Tallet A, Pomeau Y, Di Menza L. Example of a chaotic crystal: The labyrinth. Phys Rev E 2002;66:026203.
[8] Gollub JP, McCarriar AR, Steinman JF. Convective pattern evolution and secondary instabilities. J Fluid Mech 1982;125:259–81.
[9] Lesieur M. Turbulence in fluids: stochastic and numerical modelling. Dordrecht: Springer; 1987.
[10] Frisch U. Turbulence: the legacy of an Kolmogorov. Cambridge: Cambridge University Press; 1995.
[11] Callies J, Ferrari L, Klymak JM, Gula J. Seasonality in submesoscale turbulence. Nature Commun 2015;6:6862.
[12] Sasaki H, Klein P, Sasai Y. Impact of oceanic-scale interactions on the seasonal modulation of ocean dynamics by the atmosphere. Nature Commun 2014;5:5636.
[13] Schmitt JM, Kumar G. Turbulent nature of refractive-index variations in biological tissue. Opt Lett 1996;21:1310.
[14] Turitsyna EG, Smirnov SV, Sugavanam S, Tarasov N, Shu X, Babin SA, et al. The laminar-turbulent transition in a fibre laser. Nature Photon 2013;7:783.
[15] Wabnitz S. Optical turbulence in fiber lasers. Opt Lett 2014;39:1362–4.
[16] Gonzalez IRR, et al. Turbulence hierarchy in a random fibre laser. Nat Comm 2017;8:15731.
[17] Xu G, Vocke D, Faccio D, Garnier J, Roger T, Trillo S, Picozzi A. From coherent shocklets to giant collective incoherent shock waves in nonlocal turbulent flows. Nature Commun 2015;6:8131.
[18] Martínez-Prat B, Alert R, Meng F, Ignes-Mullol J, Joanny JF, Casademunt J, et al. Sagues scaling regimes of active turbulence with external dissipation. Phys Rev X 2021;11:031065.
[19] Alert R, Casademunt J, Joanny JF. Active turbulence. Annu Rev Condens Matter Phys 2022;13:143.
[20] Takeuchi KA, Sano M. Universal fluctuations of growing interfaces: evidence in turbulent liquid crystals. Phys Rev Lett 2010;104:230601.
[21] Ouyang Q, Swinney HL. Transition to chemical turbulence. Chaos 1991;1:411.
[22] Ghashghaie S, Breymann W, Peinke J, Talkner P, Dodge Y. Turbulent cascades in foreign exchange markets. Nature 1996;381:767.
[23] Lux T. Turbulence in financial markets: the surprising explanatory power of simple cascade models. Quant Finance 2010;1:632.
[24] Henn EAL, Seman JA, Roati G, Magalhaes KMF, Bagnato VS. Emergence of turbulence in an oscillating Bose–Einstein condensate. Phys Rev Lett 2009;103:045301.
[25] Zakharov VE, Lvov VS, Falkovich GE. Kolmogorov spectra of turbulence I – wave turbulence. Berlin: Springer-Verlag; 1992.
[26] Aranson IS, Kramer L. The world of the complex Ginzburg–Landau equation. Rev Modern Phys 2002;74:99.
[27] Kuramoto Y. Chemical turbulence. in chemical oscillations, waves, and turbulence. Berlin, Heidelberg: Springer; 1984.
[28] Alvarez-Garrido F, Clerc MG, González-Cortés G. Transition to spatiotemporal intermittency and defect turbulence in systems under translational coupling. Phys Rev Lett 2020;124(16):16410.
[29] Pikovsky A, Politi A. Lyapunov exponents: a tool to explore complex dynamics. Cambridge University Press; 2016.
[30] Ahlers G, Behringer PR. Evolution of turbulence from the Rayleigh-Bénard instability. Phys Rev Lett 1978;40:712.
[31] Residori S. Patterns, fronts and structures in a liquid-crystal-light-valve with optical feedback. Phys Rep 2005;416:201.
[32] A video showing spatiotemporal evolution of the measured intensity field along with auxiliary fields can be found in the Supplementary Materials. The main results are presented in the video.
[33] Egolf DA, Melnikov IV, Bodenschatz E. Importance of local pattern properties in spiral defect chaos. Phys Rev Lett 1998;80:3228.
[34] Yamada T, Kuramoto Y. A reduced model showing chemical turbulence. Progr Theoret Phys 1976;56:681.
[35] Manneville P. Statistical properties of chaotic solutions of a one-dimensional model for phase turbulence. Phys Lett A 1981;84:129.
[36] Fujisaka H, Yamada T. Theoretical study of a chemical turbulence. Progr Theoret Phys 1977;57:734.
[37] Yakhot V. Large-scale properties of unstable systems governed by the Kuramoto-Sivashinksi equation. Phys Rev A 1981;24:642.
[38] Phillips OM. The equilibrium range in the spectrum of wind-generated waves. J Fluid Mech 1958;4:426.
[39] Kuznetsov EA. Turbulence spectra generated by singularities. J Exp Theor Phys 2004;80:83.
[40] Sigeti DE. Survival of deterministic dynamics in the presence of noise and the exponential decay of power spectra at high frequency. Phys Rev E 1995;52:2443.
[41] Wietzke L, Fleischmann O, Sommer G. 2D image analysis by generalized Hilbert transforms in conformal space. In: Proceedings of European conference on computer vision. vol. 638, 2008.
[42] Grebogi C, Ott E, Pelikan S, Yorke JA. Strange attractors that are not chaotic. Physica D 1984;13:261.
[43] Clerc MG, González-Cortés G, Odent V, Wilson M. Optical textures: characterizing spatiotemporal chaos. Opt Express 2016;24:15478.
[44] Clerc MG, Petrossian A, Residori S. Bouncing localized structures in a liquid-crystal light-valve experiment. Phys Rev E 2005;71:015205.
[45] Durniak C, Taki M, Tlidi M, Ramazza P, Bortolozzo U, Kozyreff G. Modulated optical structures over a modulationally stable medium. Phys Rev E 2005;72:026607.
[46] Alvarez-Socorro AJ, Clerc MG, González-Cortés G, Wilson M. Nonvariational mechanism of front propagation: Theory and experiments. Phys Rev E 2017;95:010202.
[47] Alvarez-Socorro AJ, Clerc MG, González-Cortés G, Wilson M. Nonvariational mechanism of front propagation: Theory and experiments. Phys Rev E 2017;95:010202.
[48] Kozyreff G, Tlidi M. Nonvariational real Swift-Hohenberg equation for biological, chemical, and optical systems. Chaos 2007;17:037103.
[49] Gertsberg VL, Sivashinsky GI. Large cells in nonlinear Rayleigh-Benard convection. Progr Theoret Phys 1981;66(4):1219.
[50] Greenside HS, Cross MC. Stability analysis of two-dimensional models of three-dimensional convection. Phys Rev A 1985;31(4):2492.
[51] Skokos C. Dynamics of small solar system bodies and exoplanets. Berlin, Heidelberg: Springer; 2010.